SR Applications 1

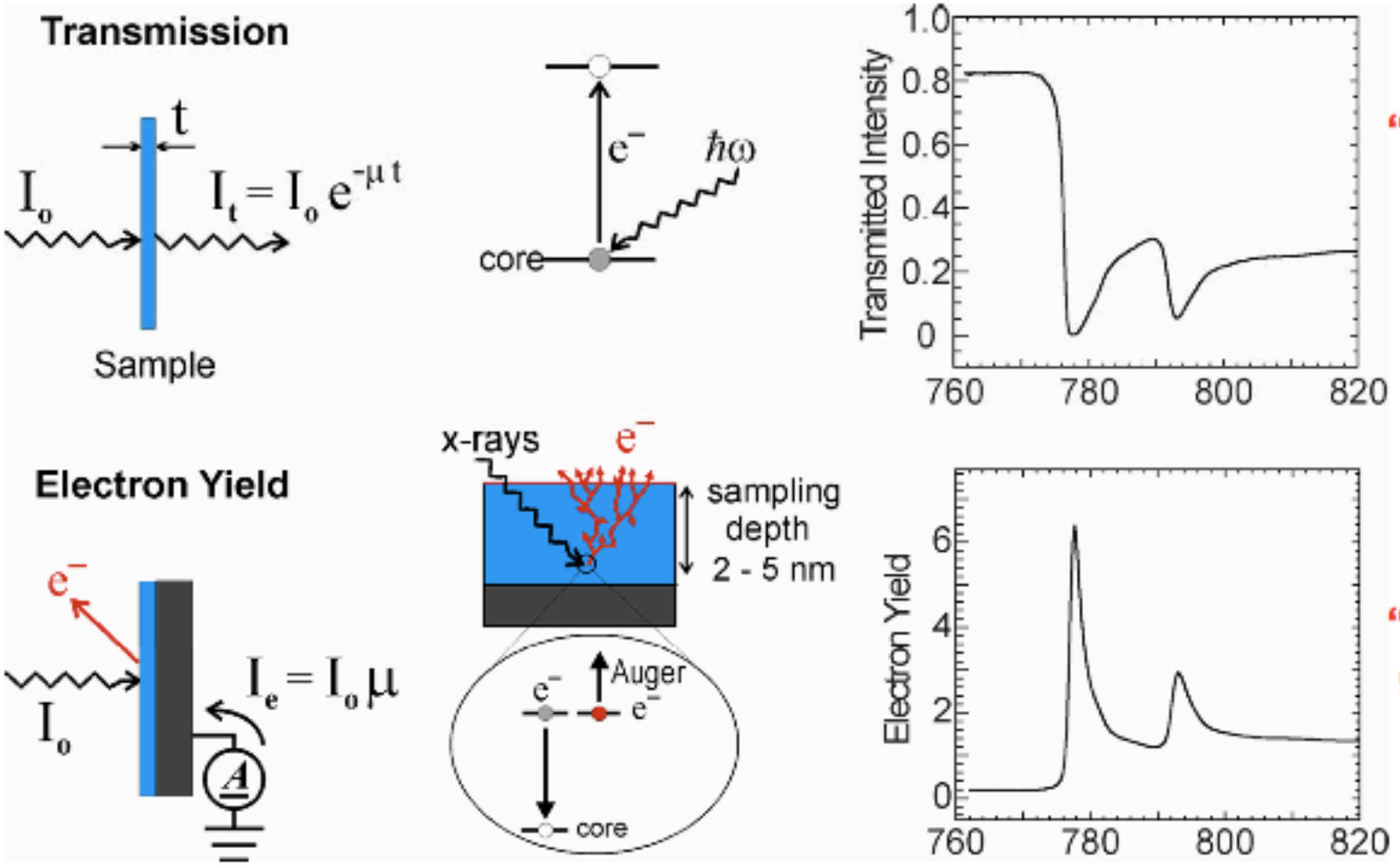

SR Applications 2

Tunable x-rays offer elemental specificity

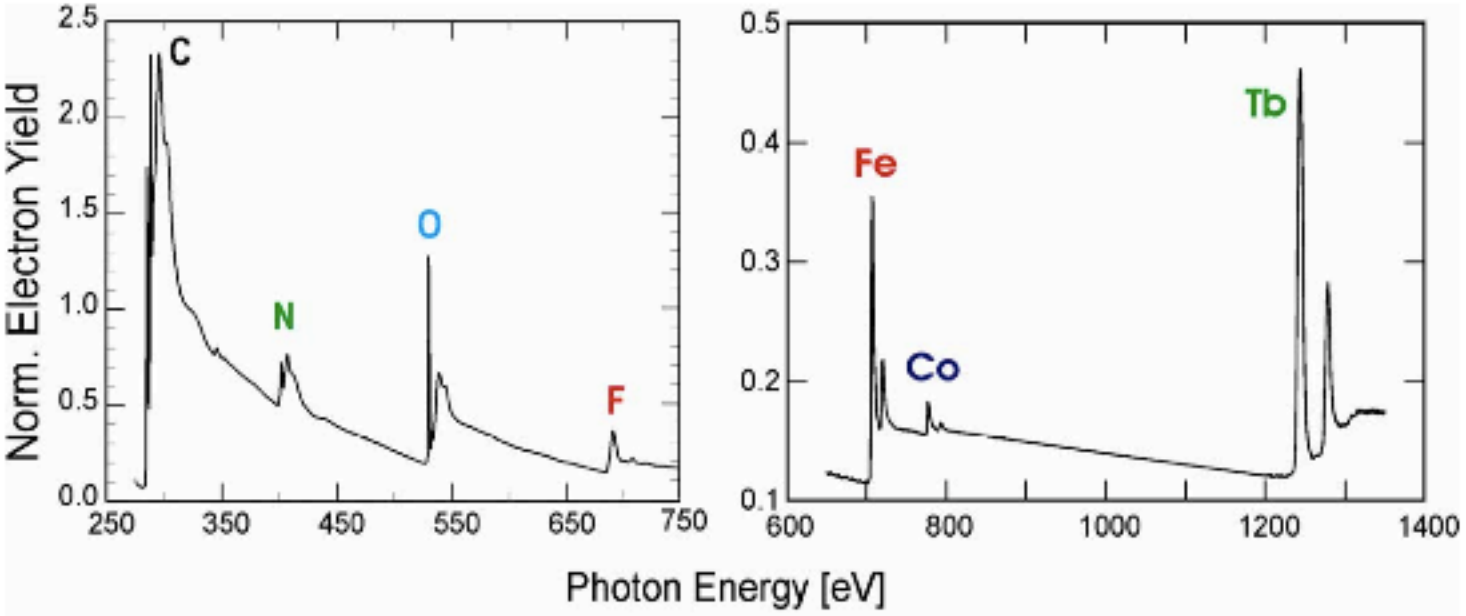

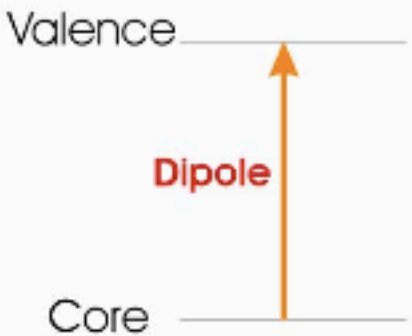

Polymers: p-orbitals
Trans. Met.: d-orbitals
Rare Earths: f-orbitals

1s K-edge
2p L edge
3d M edge

SR Applications 3

X-rays can pick materials apart: layer-by-layer

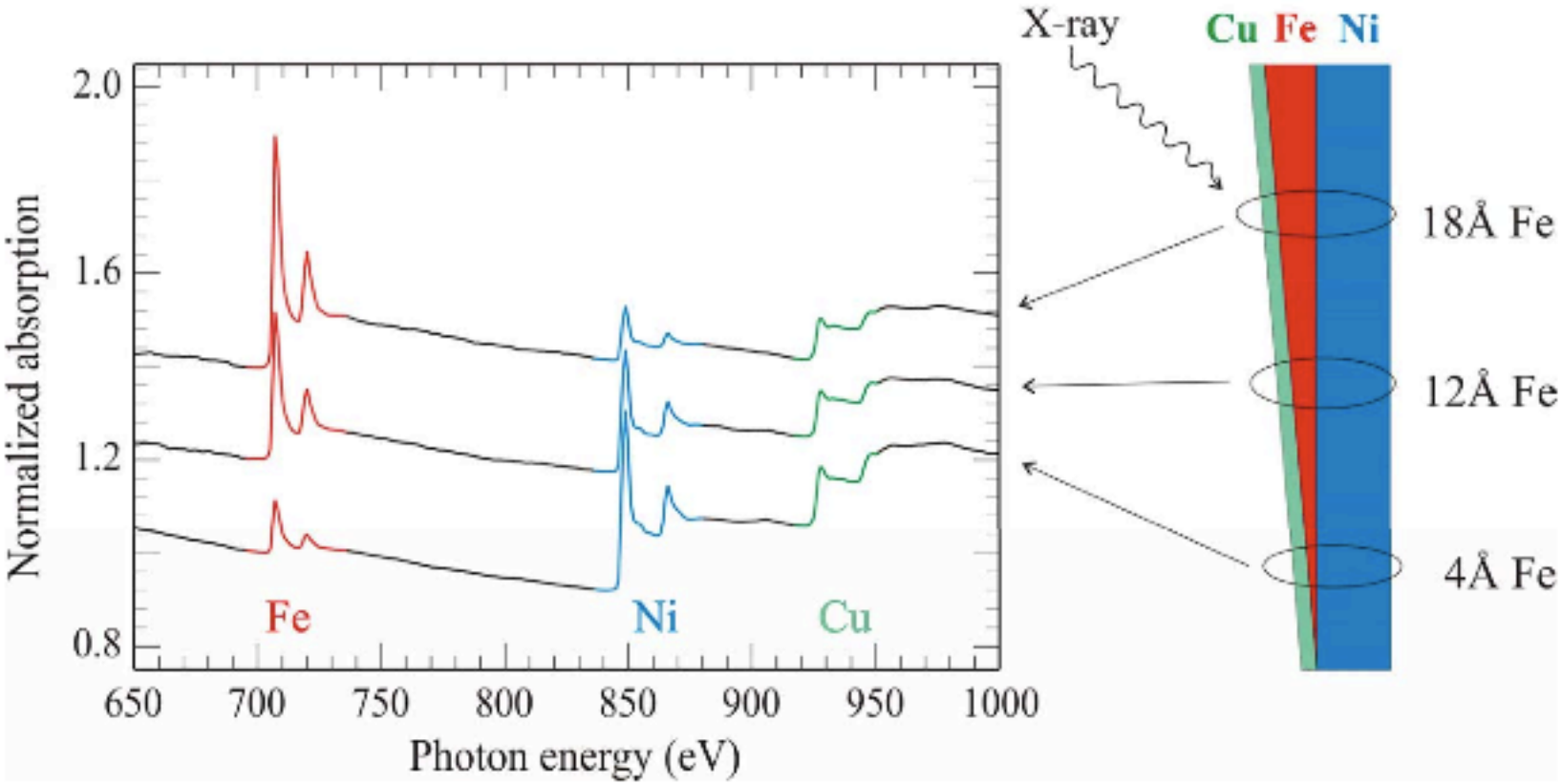

SR Applications 4

Rich "multiplet structure" reveals local bonding

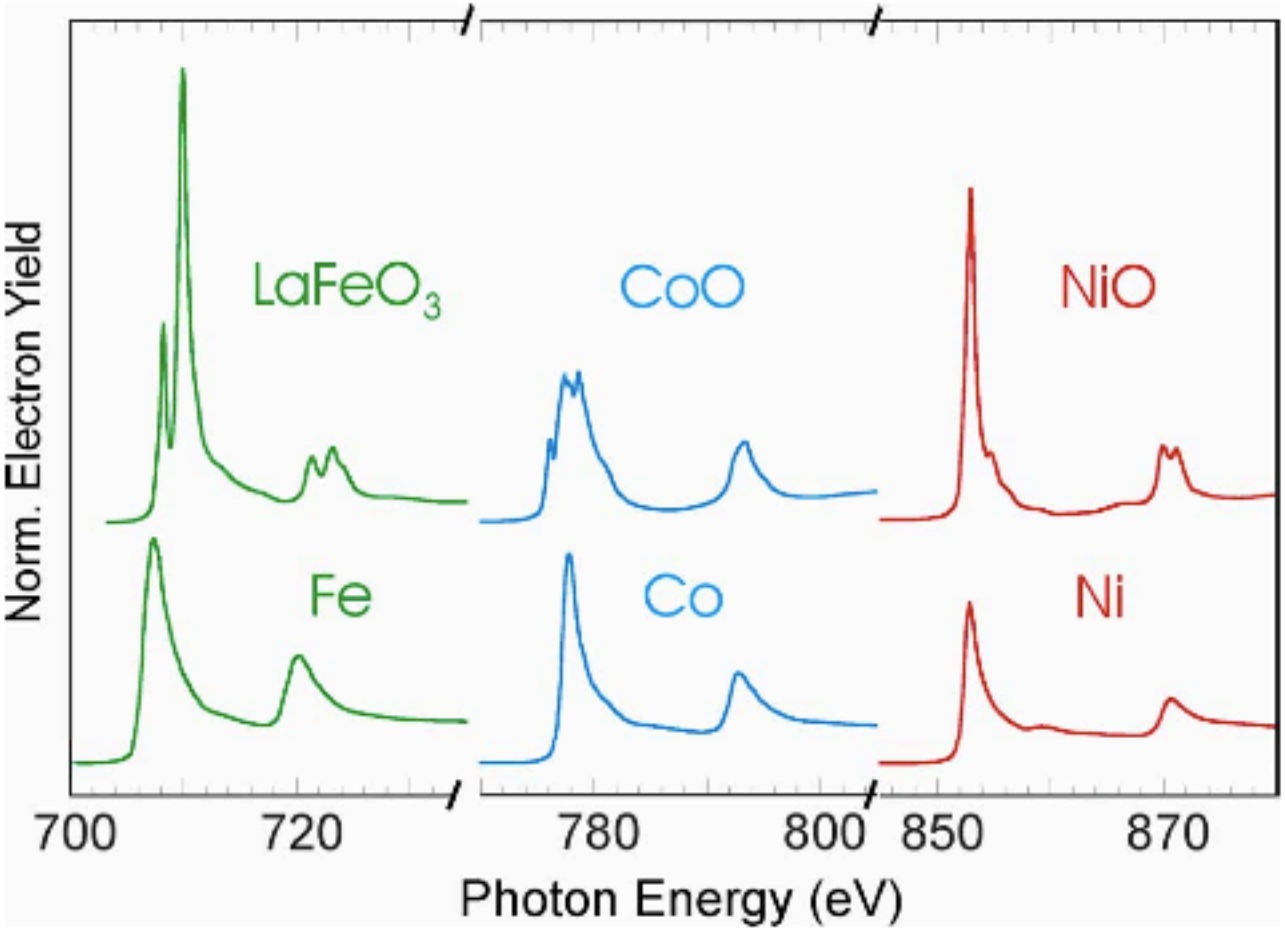

SR Applications 5

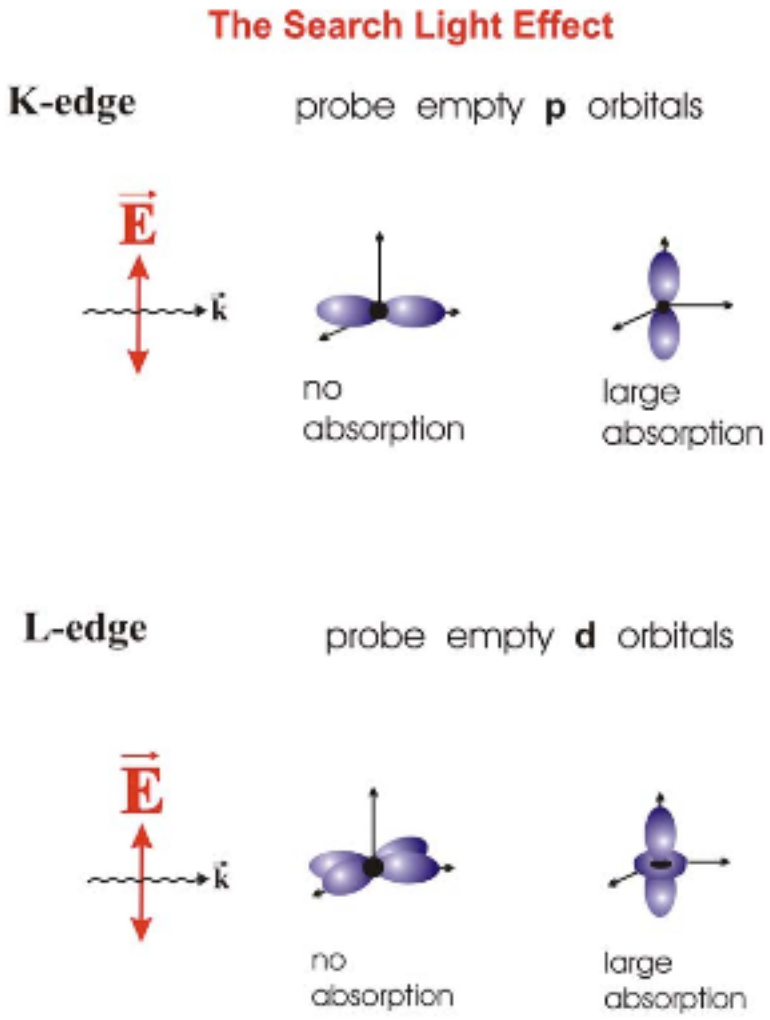

SR Applications 6

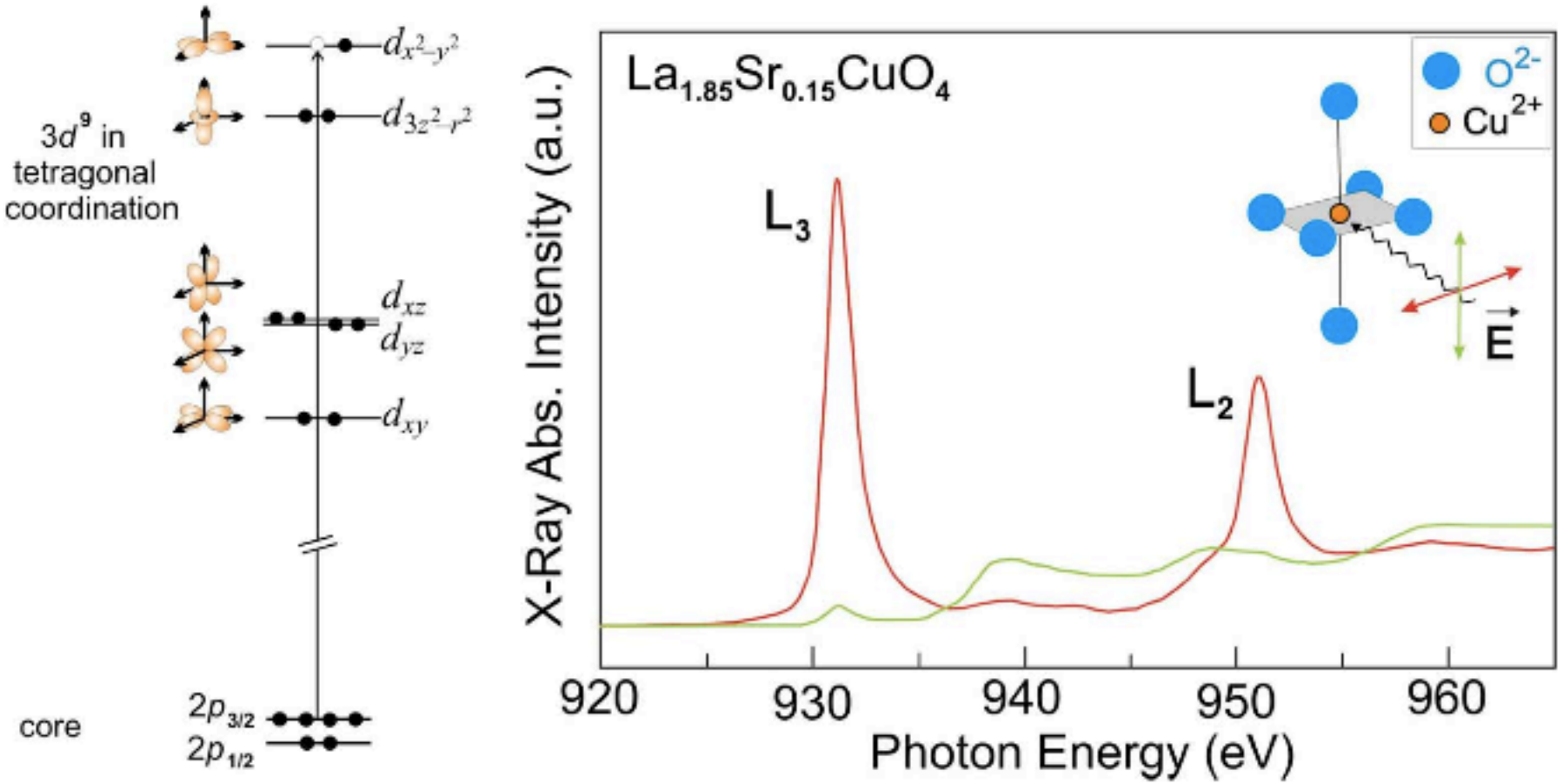

SR Applications 7

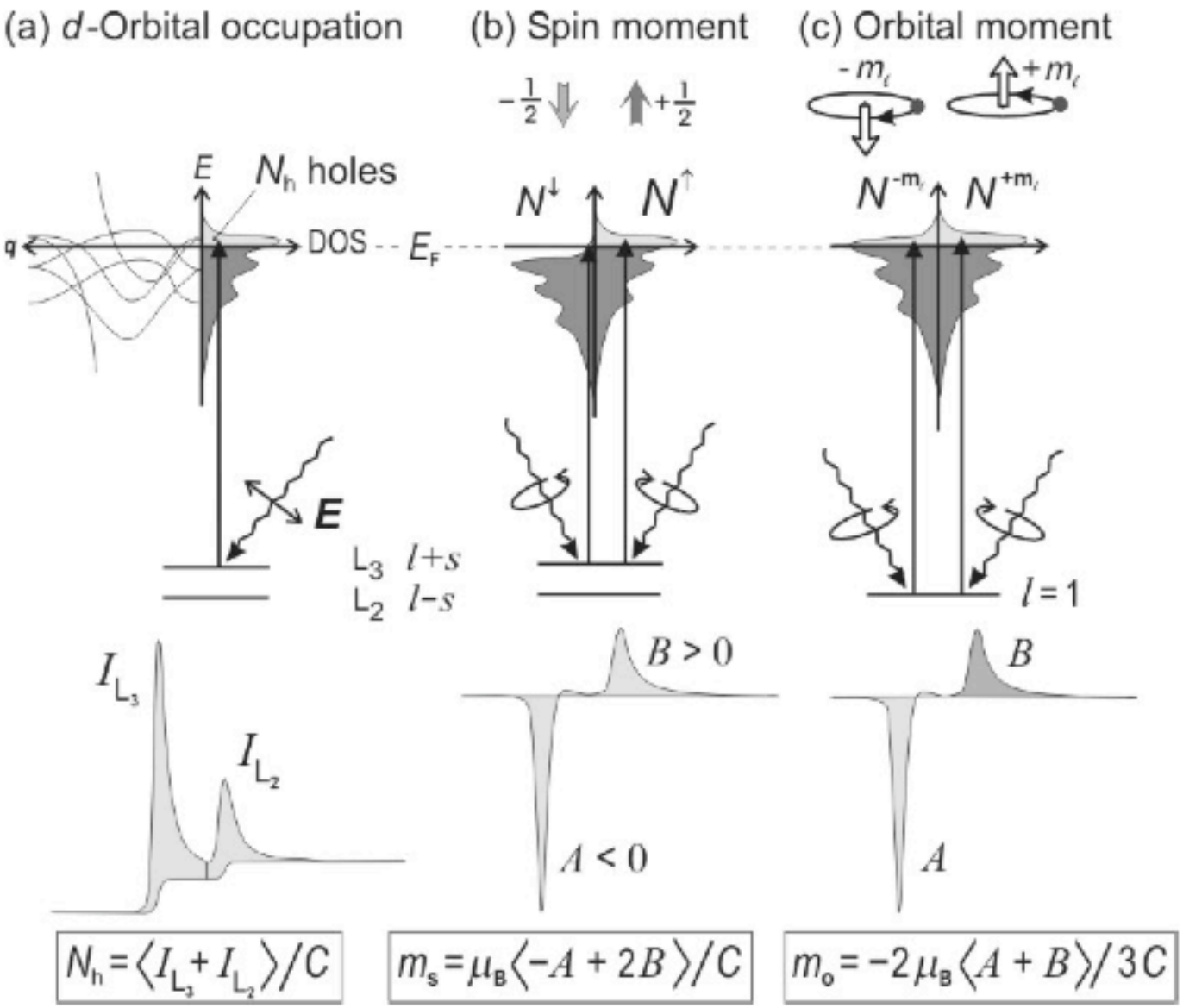

SR Applications 8

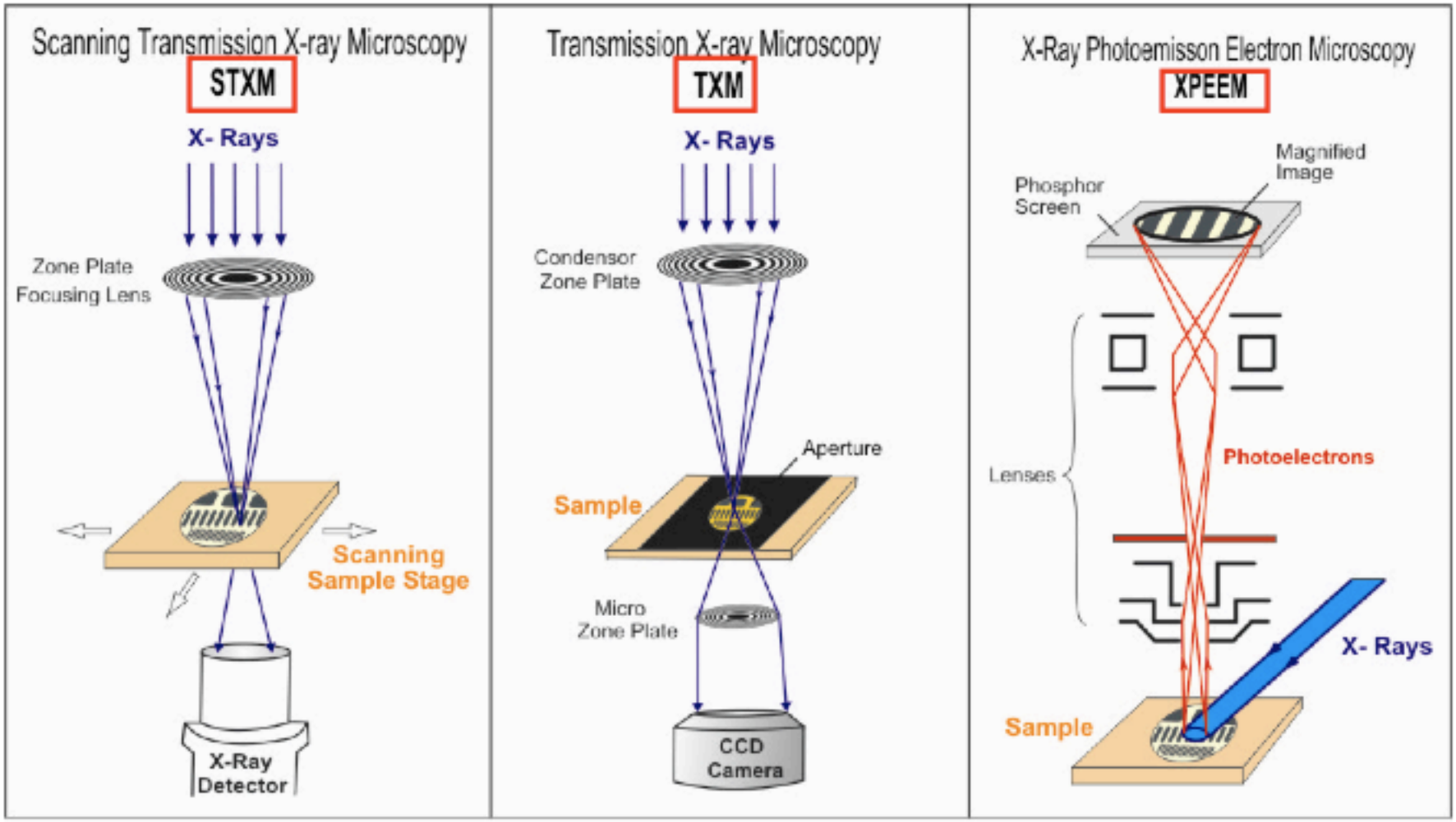

Present resolution in the 20 - 40 nm range

x-rays in / x-rays out – bulk like sensitivity

x-rays in / electrons out – near-surface sensitivity

SR Applications 9

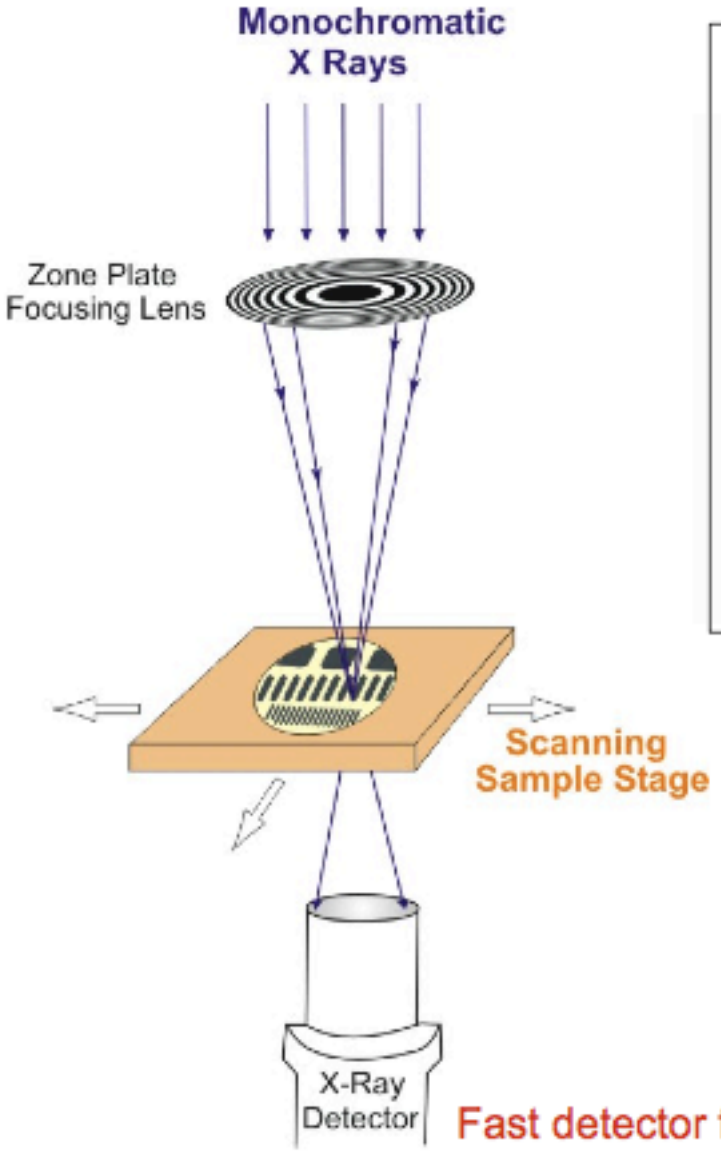

Fast detector for dynamics

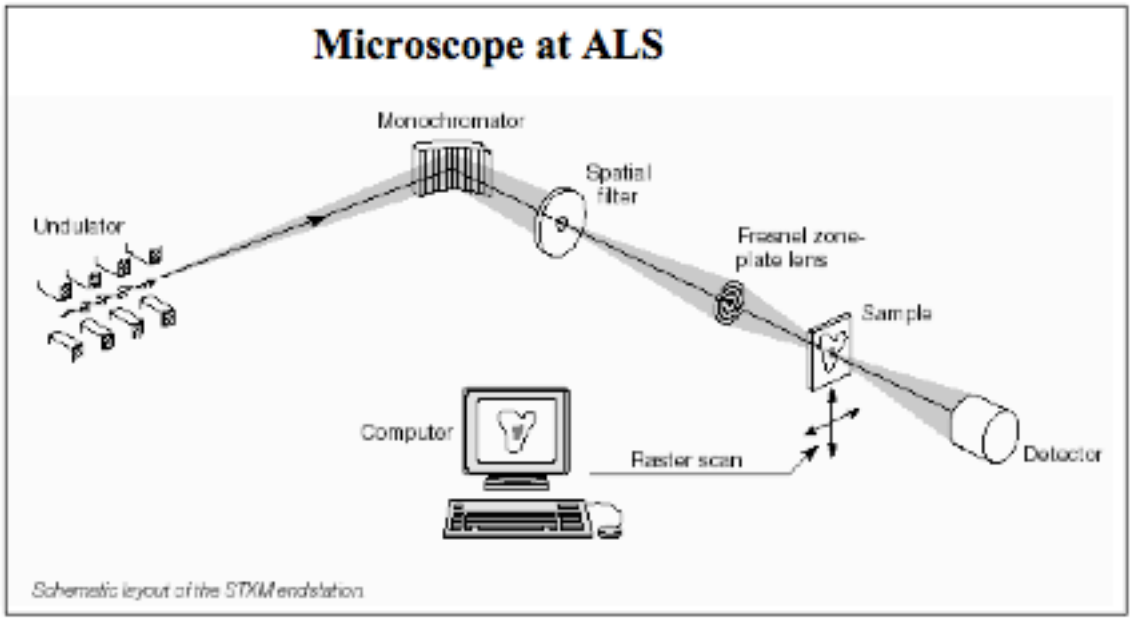

Diffraction

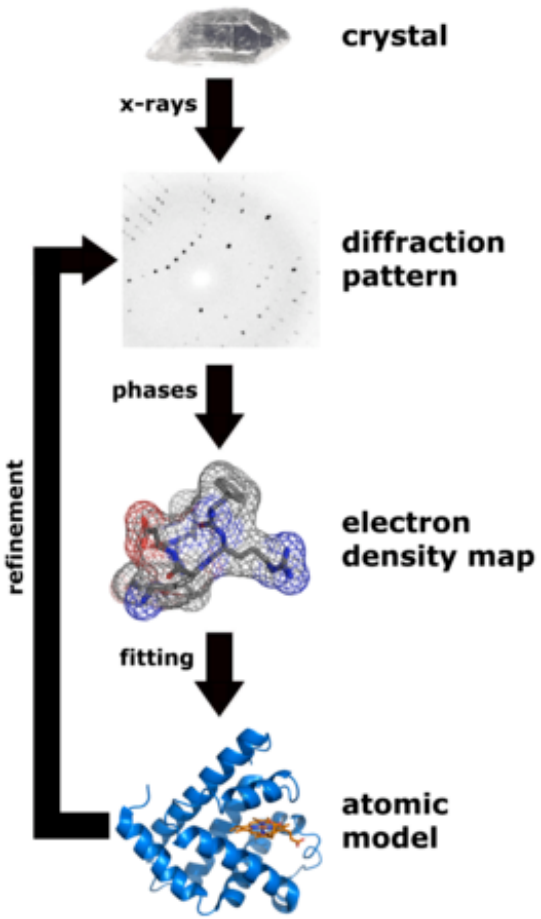

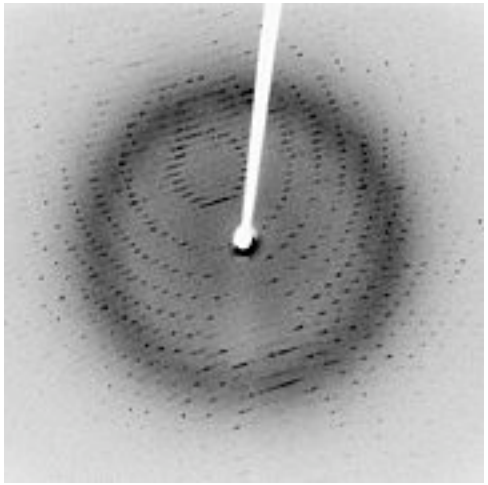

An X-ray diffraction pattern of a crystallized enzyme. The pattern of spots (called *reflections*) can be used to determine the structure of the enzyme.

$$2d\sin\theta = n\lambda$$ Bragg's law

$$\text{amplitude of scattered wave} = Ae^{i\mathbf{k}\cdot\mathbf{r}}Sf(\mathbf{r})dV$$

$$Ae^{i\mathbf{k}_{in}\cdot\mathbf{r}} \qquad e^{i\mathbf{k}_{out}\cdot(\mathbf{r}_{\text{screen}}-\mathbf{r})}$$

$$AS\int d\mathbf{r}f(\mathbf{r})e^{i\mathbf{k}_{in}\cdot\mathbf{r}}e^{i\mathbf{k}_{out}\cdot(\mathbf{r}_{\text{screen}}-\mathbf{r})} = ASe^{i\mathbf{k}_{out}\cdot\mathbf{r}_{\text{screen}}}\int d\mathbf{r}f(\mathbf{r})e^{i(\mathbf{k}_{in}-\mathbf{k}_{out})\cdot\mathbf{r}}$$

$$ASe^{i\mathbf{k}_{out}\cdot\mathbf{r}_{\text{screen}}}\int d\mathbf{r}f(\mathbf{r})e^{-i\mathbf{q}\cdot\mathbf{r}} = ASe^{i\mathbf{k}_{out}\cdot\mathbf{r}_{\text{screen}}}F(\mathbf{q}) \qquad I\sim A^2S^2\left|F(\mathbf{q})\right|^2$$

Photoelectron Spectroscopy

- **Perturbation Theory gives Fermi's Golden Rule for transition probability**

$$w = \frac{2\pi}{\hbar}\left|\langle \psi_f | H_{\text{int}} | \psi_i \rangle\right|^2 \delta(E_f - E_i - \hbar\omega)$$

- **For dipole allowed transitions,**

$$H_{\text{int}} = \frac{e}{mc}\mathbf{A}\cdot\mathbf{p}$$

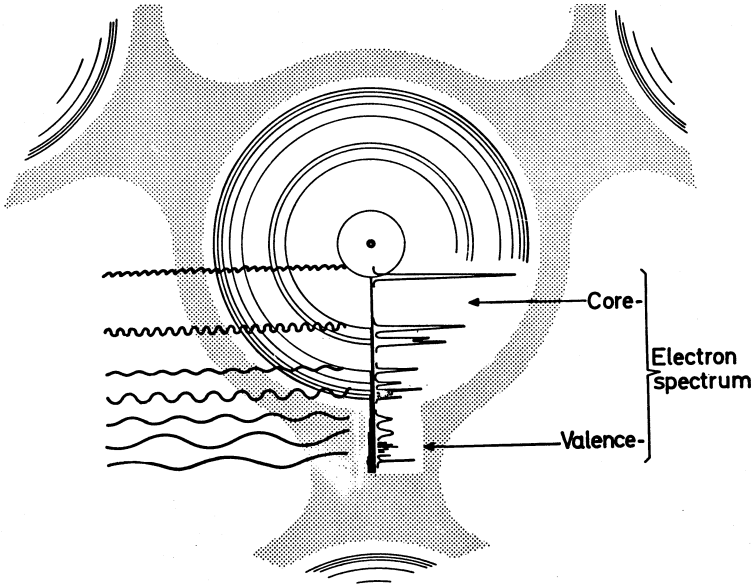

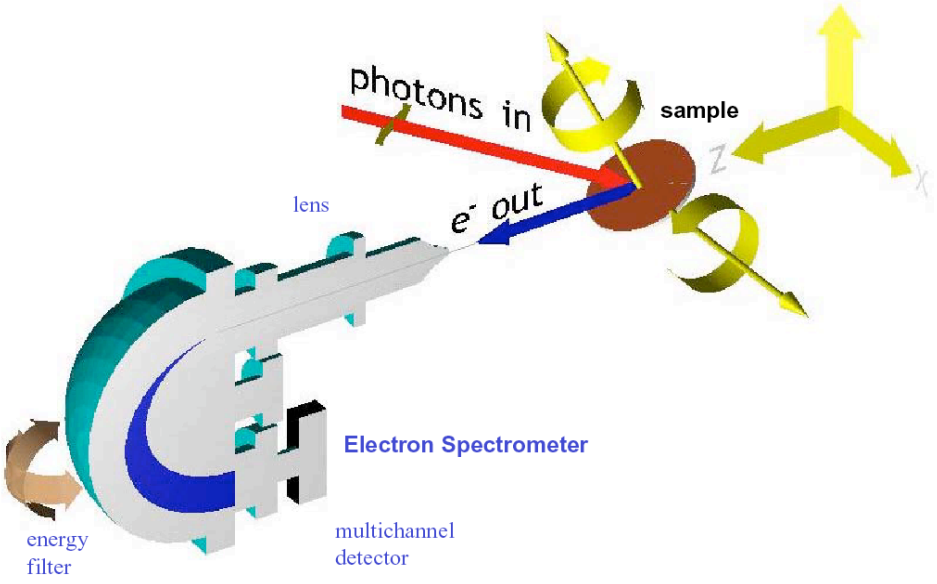

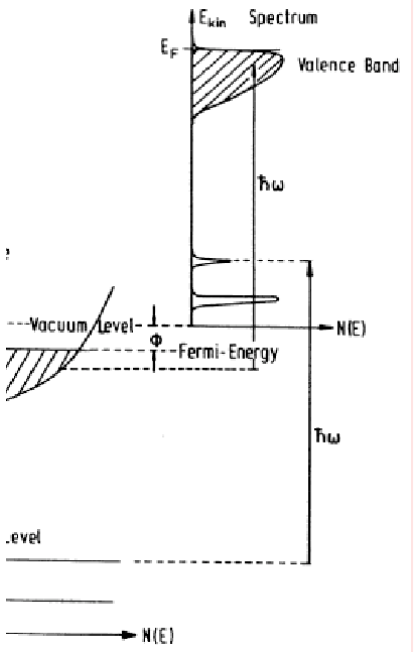

$$E_{kin} = \hbar\omega - \Phi - |E_B|$$

Measured Kinetic Energy — Measureed Photon Energy — Measured Work Function — Electron Binding Energy

Photoelectron Spectroscopy

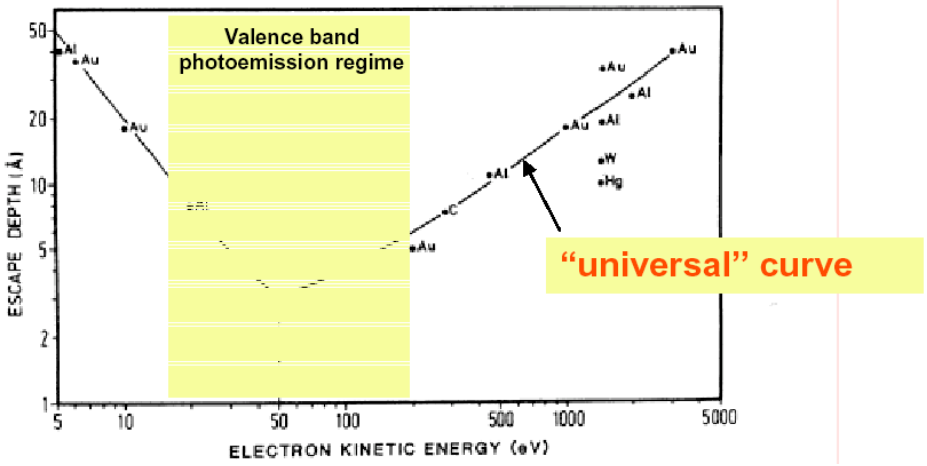

C1s, O1s and

Pt4f XPS

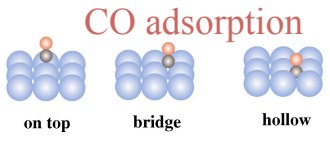

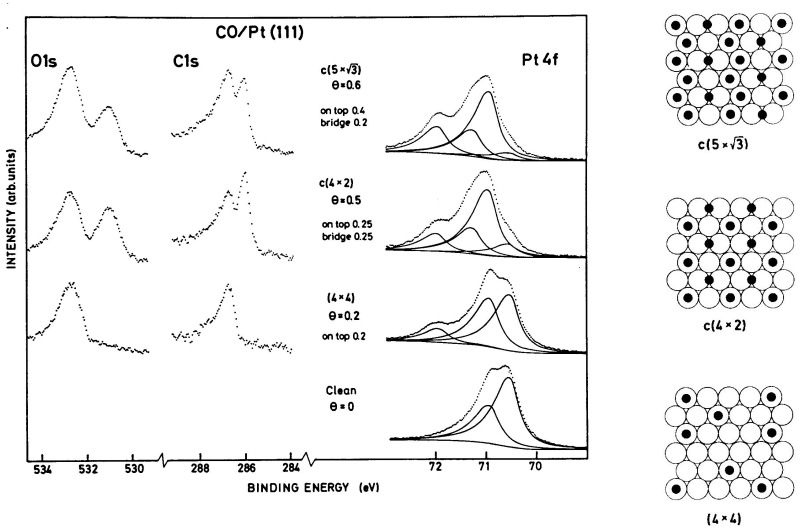

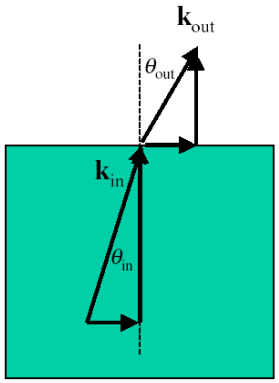

Kinematic relations

$$k_{out} = \sqrt{\frac{2m}{\hbar^2} E_{kin}}$$

$$k_{in} = \sqrt{\frac{2m}{\hbar^2}(E_{kin} + V_0)}$$

$$k_{out,\parallel} = k_{in,\parallel} \equiv k_{\parallel}$$

"Snell's Law"

$$k_{\parallel} = \sin\theta_{out}\sqrt{\frac{2m}{\hbar^2} E_{kin}} = \sin\theta_{in}\sqrt{\frac{2m}{\hbar^2}(E_{kin} + V_0)}$$

Critical angle for emission

$$(\sin\theta_{out})_{max} = \sqrt{\frac{E_{kin}}{E_{kin} + V_0}}$$

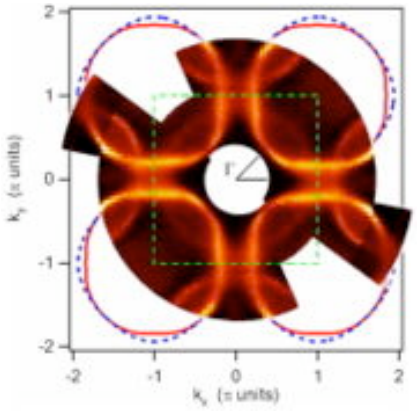

Fermi surface of BSCCO measured by ARPES. The experimental data shown as an intensity plot in yellow-red-black scale. Green dashed rectagle represents the Brillouin zone of the CuO2 plane of BSCCO.

Absorption

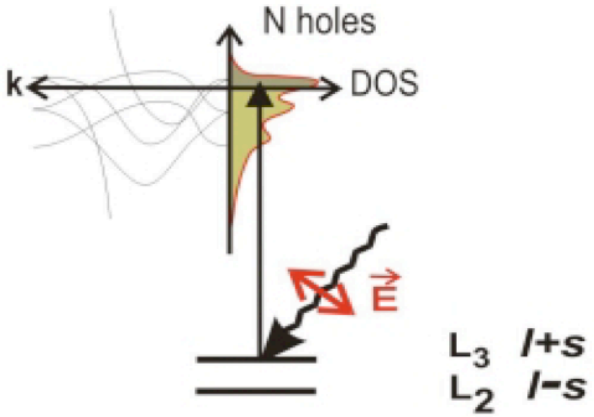

$$\left|M_{fi}\right|^2 \sim \left|\left\langle \psi_f \left| \mathbf{A}\cdot\mathbf{p} \right| \psi_i \right\rangle\right|^2 \text{ non-zero for } \begin{cases} \langle +|-|-\rangle \\ \langle +|+|+\rangle \end{cases}$$

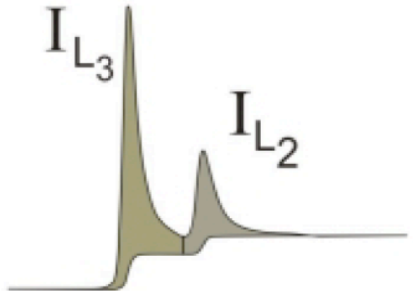

Short range order *PED and EXAFS*

Local scattering of electrons to nearest neighbor

A range of X-Ray Absorption Spectroscopy techniques are available, including X-ray Absorption Near-Edge Structure (XANES), Extended X-Ray Absorption Fine Structure (EXAFS), Resonant Inelastic X-Ray Scattering (RIXS) and X-Ray Emission Spectroscopy (XES).

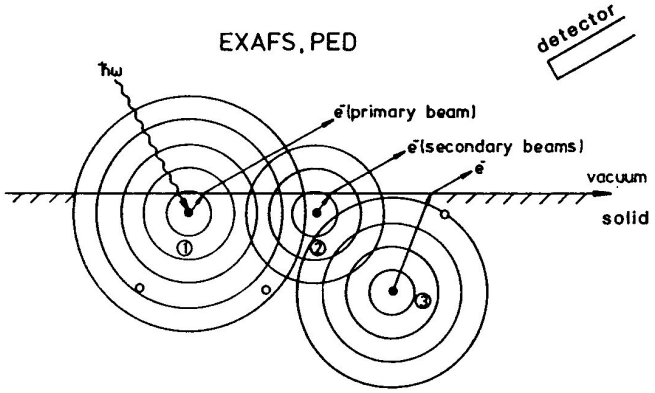

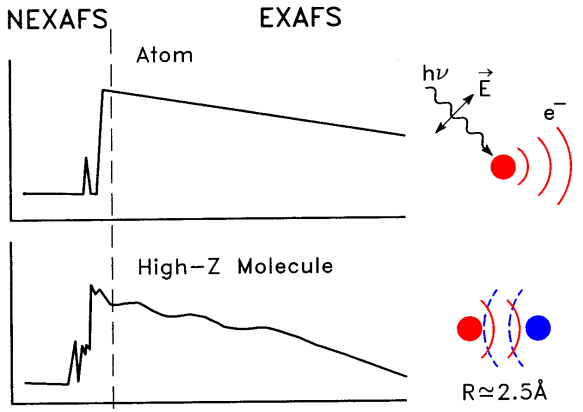

Polarization and Selection Rules

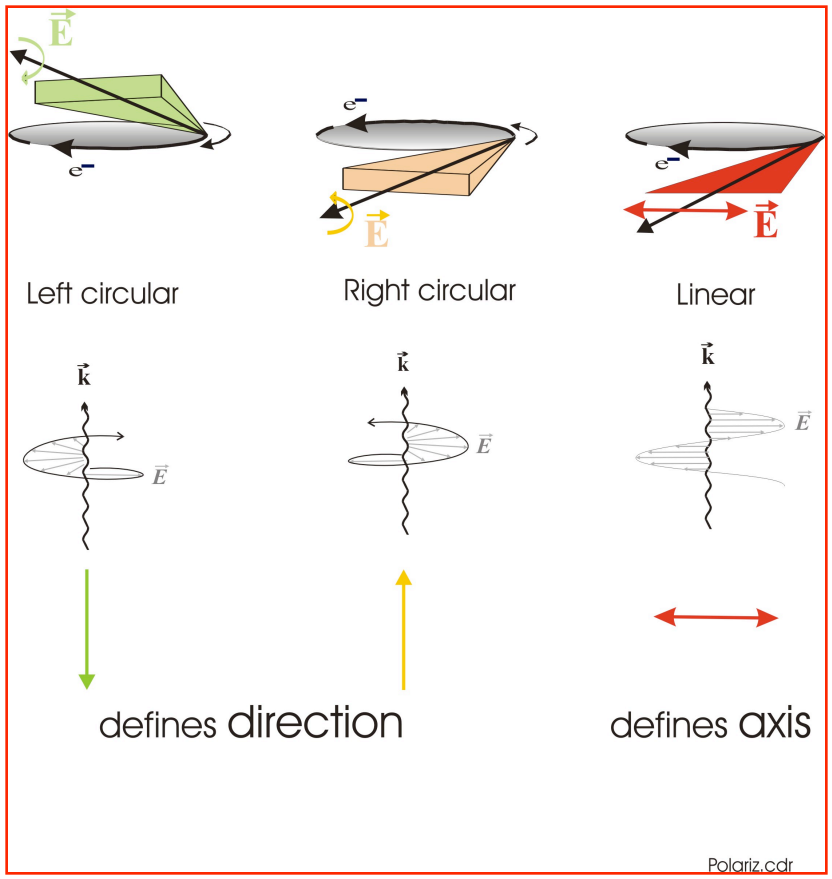

$$\mathbf{A}\cdot\mathbf{p} = D \sim \mathbf{E}\cdot\mathbf{r}$$

D = E•r is dipole operator

Linear

$D \sim z \sim r\ Y_1^0$

Right circular

$D \sim x + i\,y \sim r\,Y_1^{+1}$

Left circular

$D \sim x - i\,y \sim r\,Y_1^{-1}$

Selection rules:

$\Delta l = \pm 1,\ \Delta s = 0,\ \Delta j = 0, \pm 1$

X-ray Dichroism

X-ray Linear Dichroism

Stöhr *et al.*, Phys. Rev. Lett. **47**, 381 (1981)

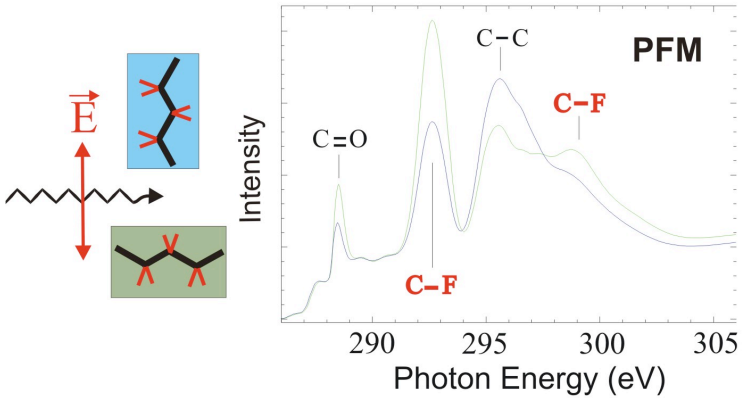

X-ray Magnetic Linear Dichroism

Van der Laan *et al.*, Phys. Rev. B **34**, 6529 (1986)

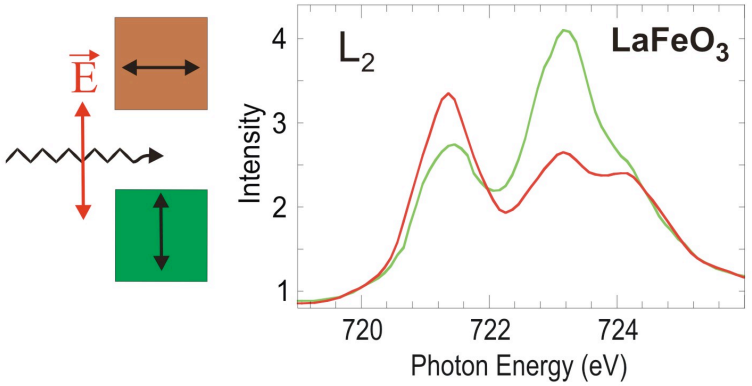

X-ray Magnetic Circular Dichroism

Schütz *et al.*, Phys. Rev. Lett. **58**, 737 (1987)

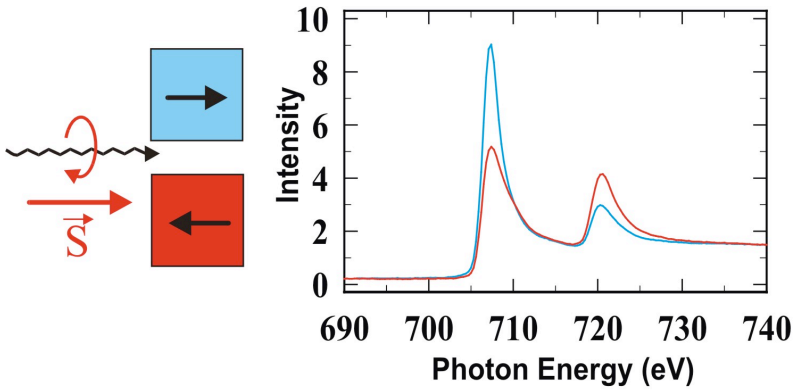

X-ray Natural Circular Dichroism

Goulon *et al.*, J. Chem. Phys. **108**, 6394 (1998)

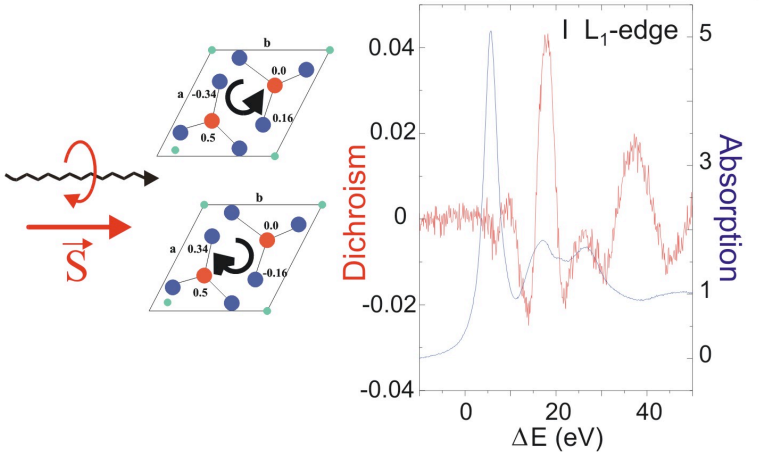

Resonant Inelastic X-ray Scattering (RIXS)

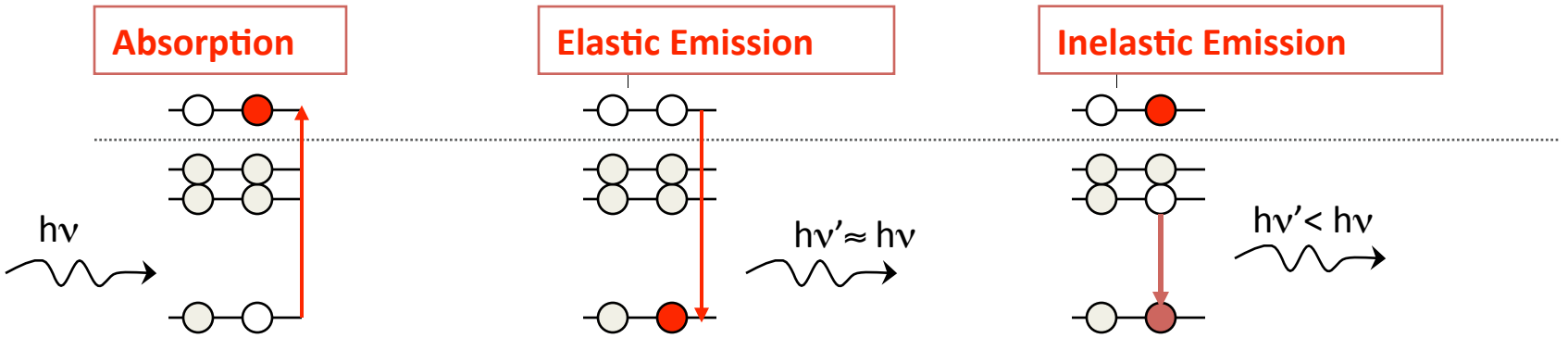

$$F(\omega,\omega') = \sum_f \left| \sum_m \frac{\langle f\ D\ m\rangle\langle m\ D\ g\rangle}{E_g + \omega - E_m - i\Gamma_m} \right|^2 \delta(E_g + \omega - E_f - \omega')$$

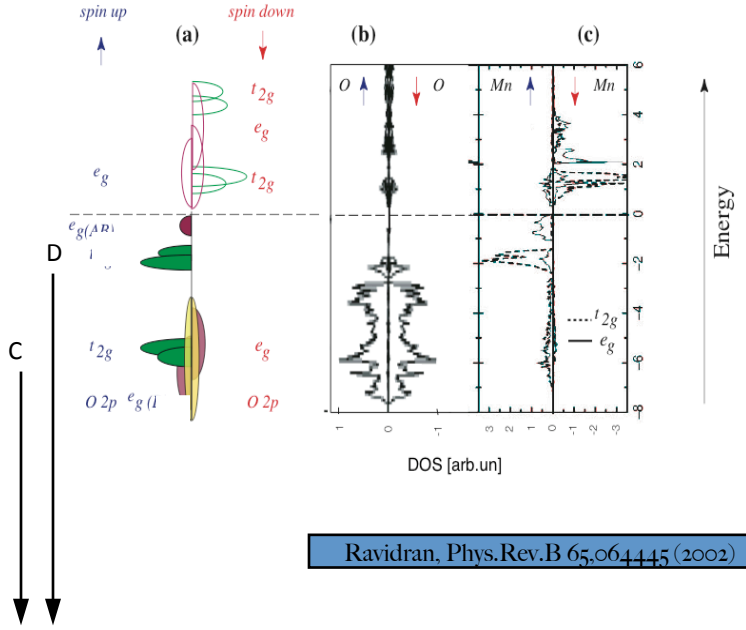

Ravidran, Phys.Rev.B 65.064445 (2002)

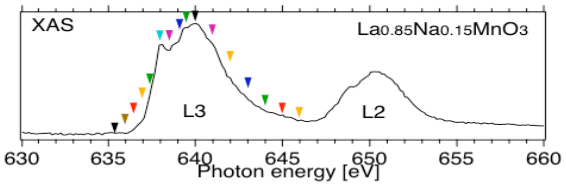

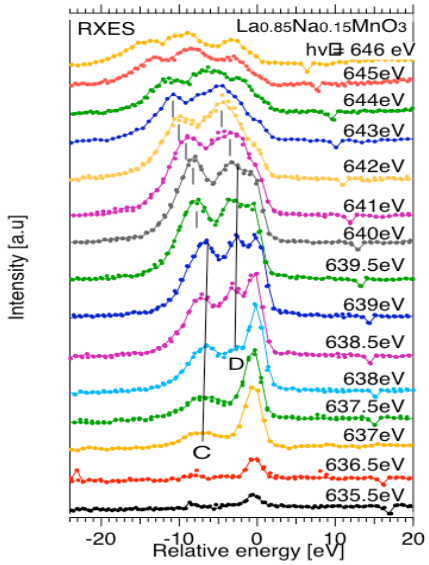

Inelastic Photon-Phonon Scattering

$S(Q,\omega)$ Dynamic Structure Factor

Courtesy C. Masciovecchio -ELETTRA

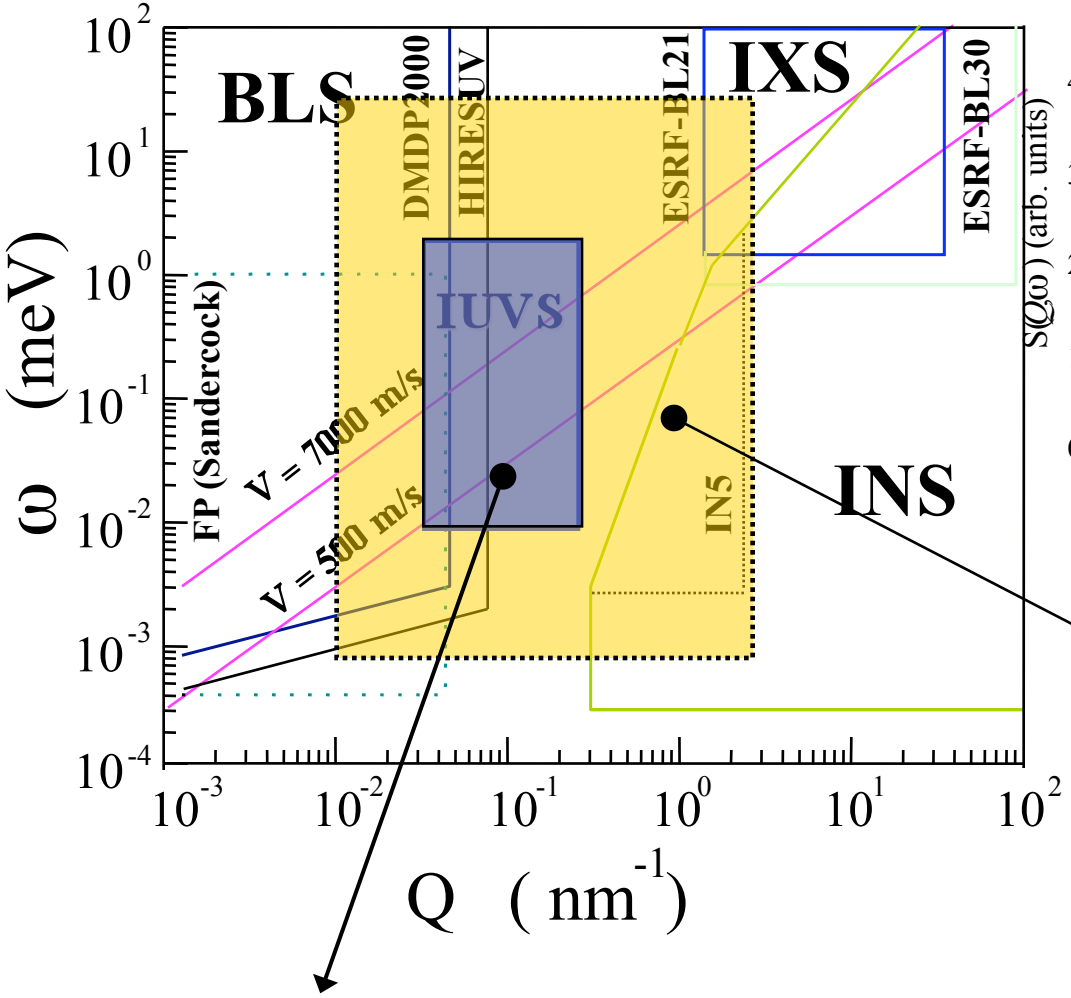

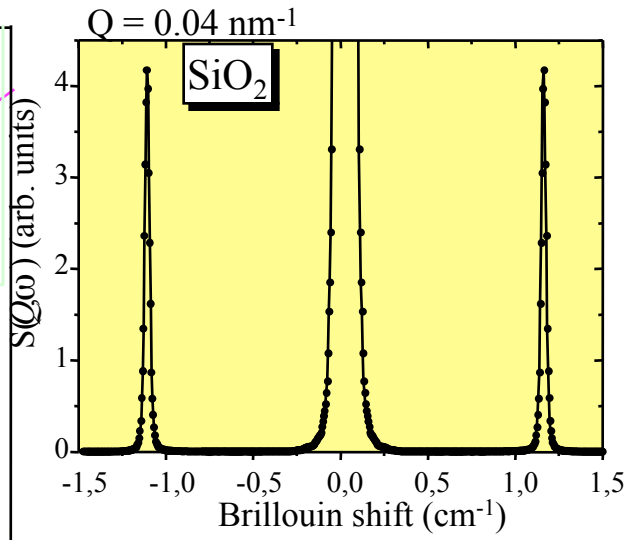

$F(\mathbf{Q},t)$

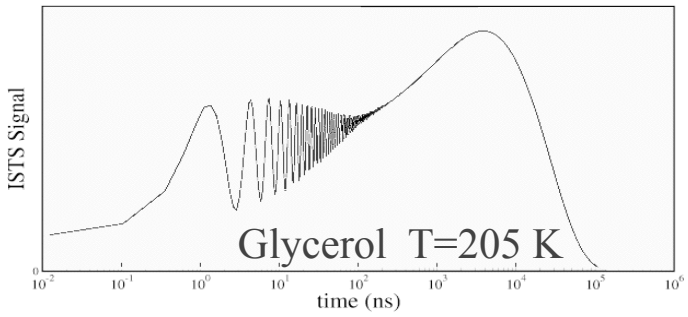

IUVS Status @ 14:00

Coherent Imaging

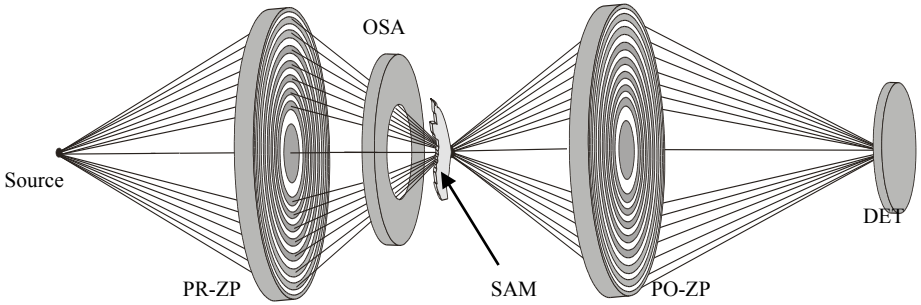

Figure . Optical scheme of TwinMic.

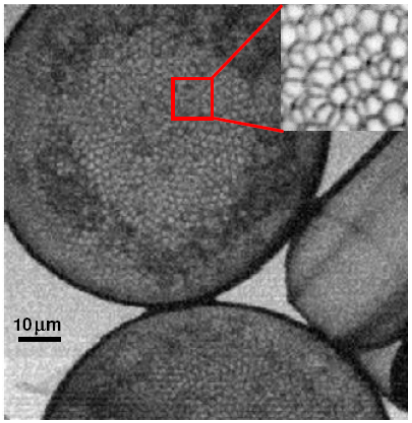

Figure 3. Scanning mode

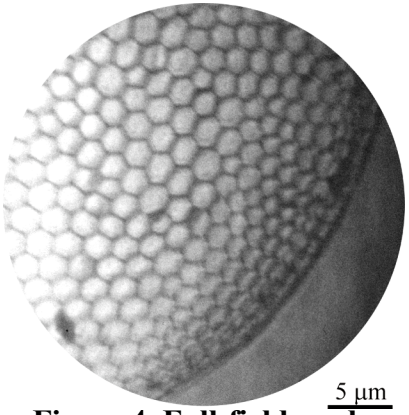

Figure 4. Full-field mode.

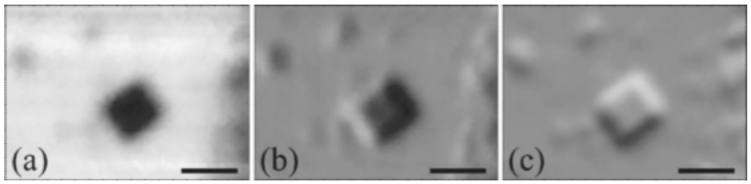

FIG. 2. Three images of a magnesium oxide cube taken with x rays of energy of ~1280 eV. The scale bar is 2 μm. The images were generated from data acquired in a single STXM scan of the sample: (a) absorption image obtained from the sum signal, (b) the *X* component of the first-moment signal, and (c) the *Y* component of the first-moment signal.

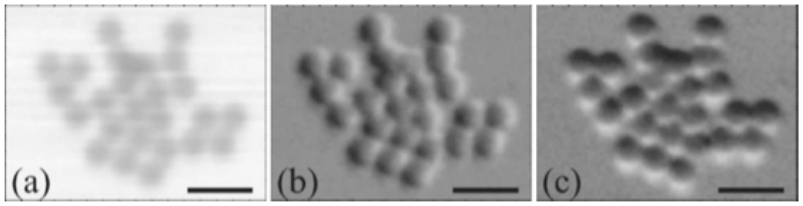

FIG. 3. Three images of a cluster of 1 μm diameter polystyrene spheres taken with x rays of energy of ~520 eV. The scale bar is 2 μm. The images were generated from data acquired in a single STXM scan of the sample: (a) absorption image obtained from the sum signal, (b) the *X* component of the first-moment signal, and (c) the *Y* component of the first-moment signal.

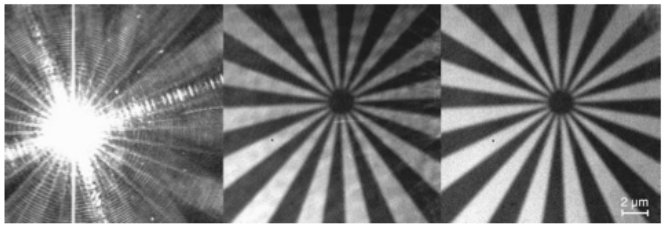

Fig. 4. X-ray microscope images of a Siemens star test pattern (smallest feature size, 400 nm period). Left, image obtained without a condenser; strong diffration artifacts are visible. Center, image with a condenser but with interference artifacts present. Right, image with a condenser and with interference artifacts removed by source vibration. No image processing, but dark image subtraction was performed on the data.

TwinMic on BACH-ELETTRA

What Keeps Bugs from Being Bigger?

Does the tracheal system actually limit how big insects can be? A recent article based on research carried out at X-ray Operations and Research beamline 1-ID at the Argonne Advanced Photon Source (APS), and published in the Proceedings of the National Academy of Sciences, helps confirm this hypothesis and provides a specific explanation for what limits size in beetles: the constriction of the tracheal tubes leading to the legs.

This study is a first step toward understanding what controls body size in insects. It's the legs that count in the beetles studied here, but what matters for the other hundreds of thousands of beetle species, and millions of insect species overall, is still an open question.

Alexander Kaiser, C. Jaco Klok, John J. Socha, Wah-Keat Lee, Michael C. Quinlan, and Jon F. Harrison, " Increase in tracheal investment with beetle size supports hypothesis of oxygen limitation on insect gigantism," Proc. Nat. Acad. Sci. USA **104**(32), 13198 (August 7, 2007).

The Initiation of Bacterial DNA Replication

At the beginning of replication, ATP binds with DnaA, causing it to change from a monomer to a large oligomeric complex consisting of DnaA monomers bound to a series of DnaA "boxes" (9-base-pair sequences). Although this DnaA/DnaA-box interaction is highly conserved in all bacteria, the mechanism by which ATP activates DnaA oligomerization has been poorly understood. However, University of California, Berkeley, researchers using ALS Beamline 8.3.1 have determined the structure of ATP-bound DnaA from the bacterium *Aquifex aeolicus.* Using data collected from a single crystal, they assembled a high-resolution model of an ATP-bound DnaA molecule using an ATP analog (AMP-PCP). Each asymmetric unit contains four structurally similar DnaA molecules arranged in a head-to-tail manner.

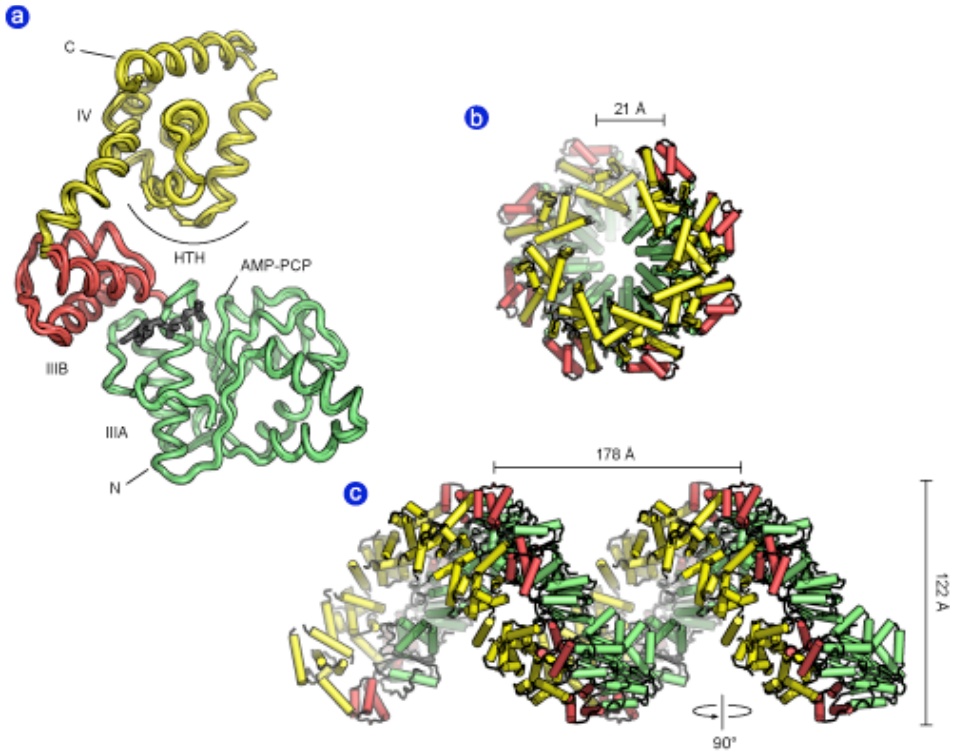

Publication about this research: J.P. Erzberger, M.L. Mott and J.M. Berger, "Structural basis for ATP-dependent DnaA assembly and replication-origin remodeling," *Nat. Struct. Mol. Biol.* **13**, 665 (2006).

Direct Evidence of Dirac Fermions in Graphite

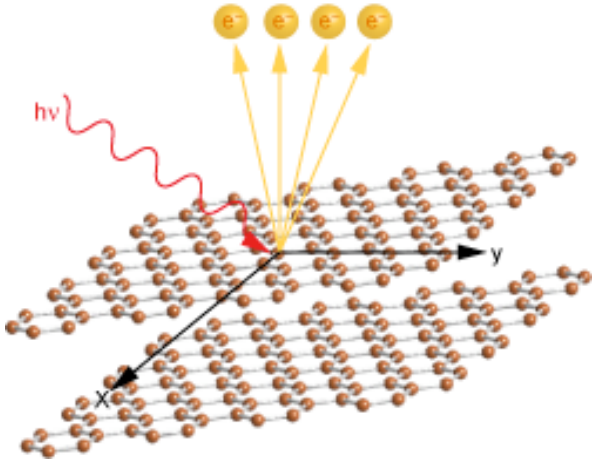

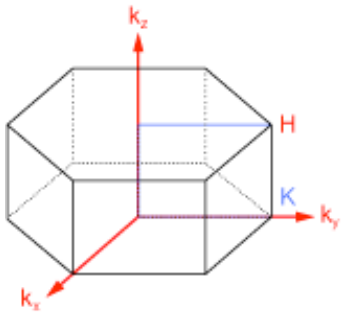

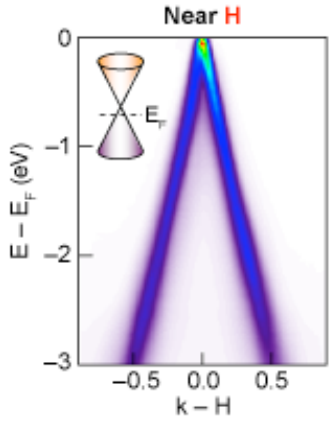

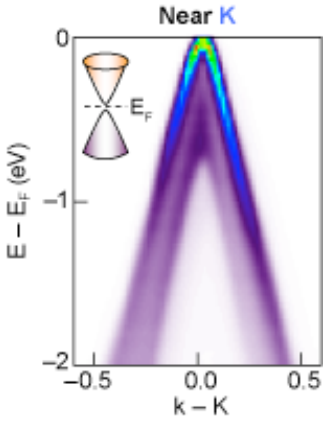

An electron moving through a conventional solid is often described as having a small but finite effective mass (m*) that takes into account the drag on its momentum from the surrounding crystal lattice as well as from interactions with other particles. The energy (E) of such an electron depends quadratically on its momentum (p), as given by the equation E = p2/2m*. In graphene, however, it has been discovered that electrons behave as if they are massless, "relativistic" particles (like photons traveling in free space at the speed of light) that exhibit a linear dispersion relationship given by the equation E = vk, where the wavenumber (k) represents momentum and the Fermi velocity (v) stands in for the speed of light. Because these electrons obey the Dirac equation—a description of fermions (e.g., electrons) that combines quantum mechanics with special relativity—they are called Dirac fermions.

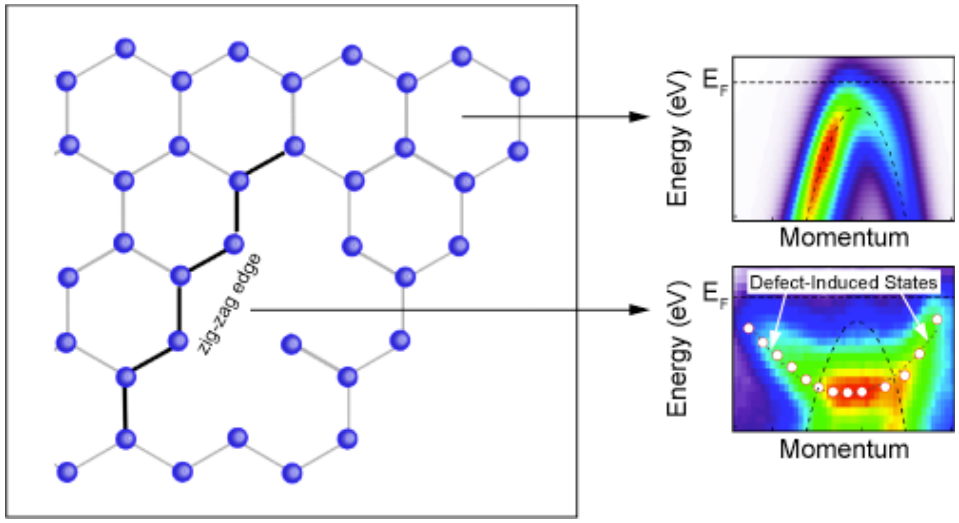

Publication about this research: S.Y. Zhou, G.-H. Gweon, J. Graf, A.V. Federov, C.D. Spataru, R.D. Diehl, Y. Kopelevich, D.-H. Lee, S.G. Louie, and A. Lanzara, "First direct observation of Dirac fermions in graphite," *Nature Physics* **2**, 595 (2006).

Surface Orbital 'Roughness' in Colossal Magnetoresistive Oxide

Transition metal oxide compounds containing a mixed-valence of Mn3+ and Mn4+, known as manganites, represent an ideal system to address the role of the surface, because all the relevant degrees of freedom - charge, spin and orbital - play an active role in determining the ground state. In particular, the orbital structure is very important for determining both the magnetic and electronic properties of the manganites. As a result, manganites are exquisitely sensitive to perturbations, and hence can be expected to exhibit relatively large surface effects. In the November 18, 2007 issue of *Nature Materials*, researchers from the Institute of Materials Structure Science, KEK (Japan), the Institut Neel/Université Joseph Fourier (France), Brookhaven National Laboratory, and Ames Laboratory, describe how the orbital structure at the surface is considerably rougher than that found in the bulk. These researchers used grazing incidence surface x-ray scattering at beamline X22C at the National Synchrotron Light Source and µCAT/X-ray Operations and Research beamline 6-ID-B at the APS, to observed the first signal of the surface x-ray scattering from the ordering (or lack thereof) of the Mn3+ 3*d* electron orbitals. Quantitative modeling of the newly discovered "orbital truncation rods," which result from the arrangement of orbitals at the surface, shows that the Mn *d* orbitals order parallel to the surface over a length scale only one-fourth of that found previously found in the bulk. Perpendicular to the surface, this orbital layer is quite rough, with "orbital steps" deviating from the average surface height by one-half the length of the chemical unit cell.

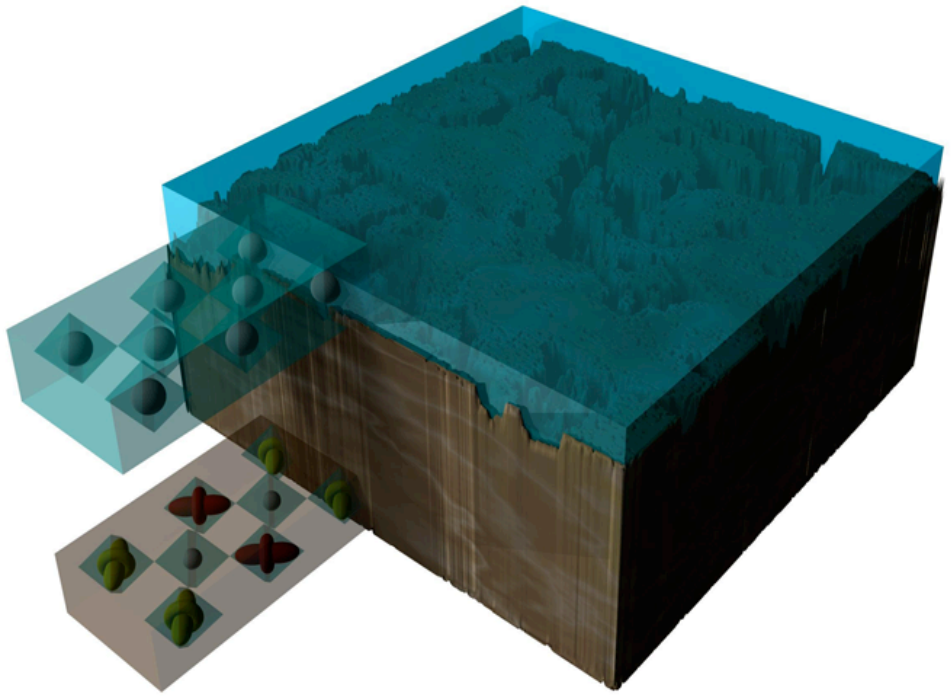

See: Y. Wakabayashi, M.H. Upton, S. Grenier, J.P. Hill, C.S. Nelson, J.-W. Kim, P.J. Ryan, A.I. Goldman, H. Zheng, and J.F. Mitchell, "Surface effects on the orbital order in the single layered manganite La0.5Sr1.5MnO4" *Nature Materials* advance online publication. Published online November 18, 2007. (doi:10.1038/nmat2061)

Locating atoms in a quasi-crystals

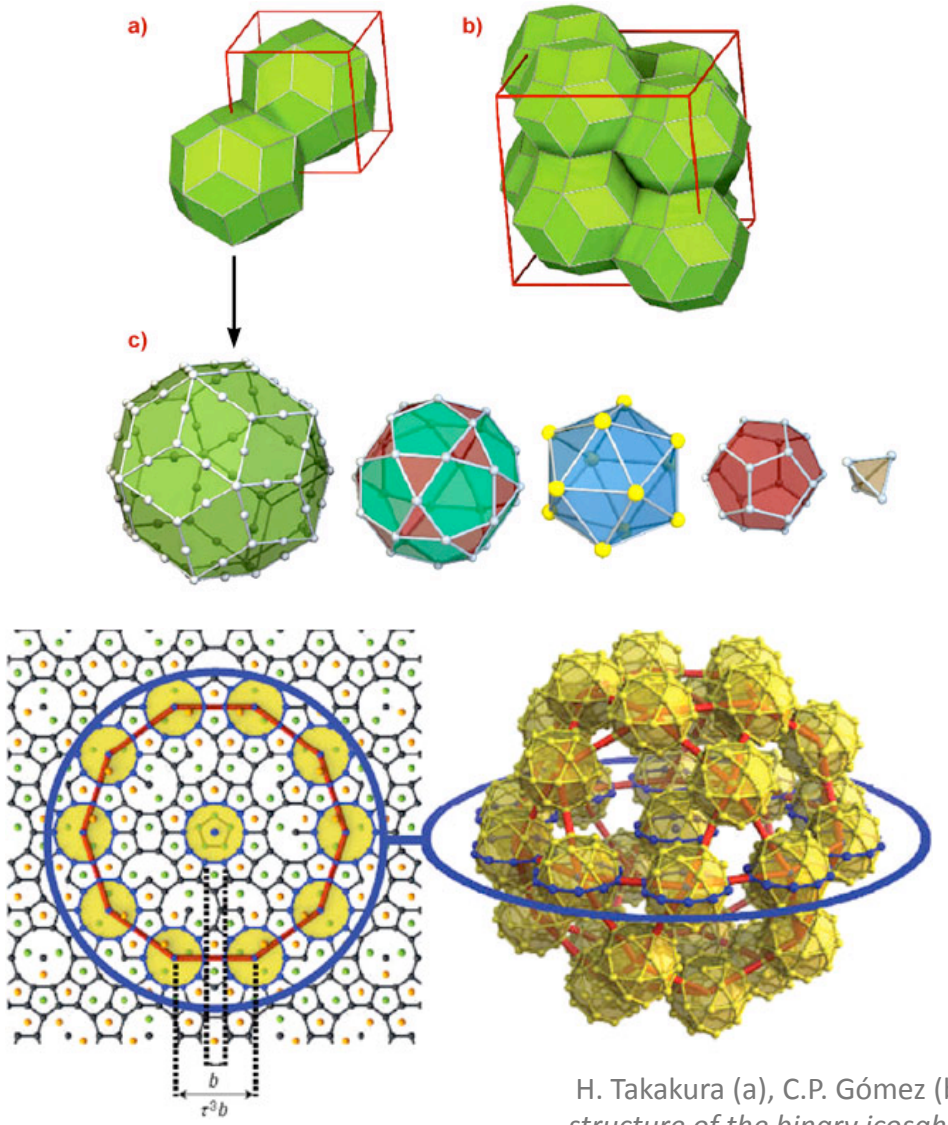

The discovery of the icosahedral phase of Cd5.7Yb by Tsai and co-workers [2] was a breakthrough. Indeed this is the first binary quasicrystal, which makes structural analysis much simpler. There is also good contrast for X-ray scattering between the Cd and Yb atoms. Finally, there are two so-called periodic approximants, which can be synthesised with chemical compositions and atomic structure very close to that of the principal quasicrystal. The structure of the approximant crystals is described by a periodic packing of a large structural unit with icosahedral symmetry, whose external shell is a triacontahedron. This forms an atomic cluster which is chemically extremely well ordered, with Yb atoms sitting on the vertices of an icosahedron. The clusters are densely packed and connected along the 2-fold and 3-fold axis, where they interpenetrate.
The structure of the icosahedral CdYb quasicrystal has been solved using X-ray diffraction data collected on the ESRF -D2AM beamline (BM02).

H. Takakura (a), C.P. Gómez (b), A. Yamamoto (c), M. de Boissieu (d), A.P. Tsai (b), *Atomic structure of the binary icosahedral Yb-Cd quasicrystal*, *Nature Materials* **6**, 58-63 (2007).

Photon parameters versus experiments

Science Opportunities	Photon Attributes						
	Coherence	Brilliance (average)	Spatial Resolution (<1 nm)	Time Resolution (<1 ps)	Peak Brilliance	Energy Resolution	Polarization (circular, linear)
Nanoparticle spectroscopy for solar cells	Nano-XPS			Charge-carrier dynamics spectroscopy			
Charge-transfer dynamics in photosynthesis				Scattering and spectroscopy to identify and control individual steps			
Battery stress and degradation	Functional imaging and spectroscopy					X	
Magnetic quantum dot materials			Imaging femtosecond magnetization dynamics				X
Understanding and development of novel superconductors		Spatially resolved electronic characterization Nano-ARPES, RIXS				X	
Chemistry at the surface of mineral particles	Imaging structure and function of mineral particles in a wet environment					X	
Catalysis and chemistry		Monitor catalysts with atomic resolution under process conditions		"Movies of a chemical reaction," femtosecond spectroscopy and scattering			
Life sciences			Flash imaging of function at the cellular level				
	3-D mapping of DNA conformations						X
	Imaging and spectroscopy of enzyme chemistry					X	
Nano-materials	X	EXAFs of clusters			Spectroscopic characterization and imaging of individual clusters		
Quantum control				Resolving and controlling electron dynamics			
Extreme environments				X-ray imaging of plasma processes